Journal of
Manufacturing and Materials Processing

MDPI

Article

Multi-Response Optimization and Influence of Expanded Graphite on Performance of WEDM Process of Ti6Al4V

Jay Vora [1], Yug Shah [1], Sakshum Khanna [2], Vivek K. Patel [1], Manoj Jagdale [3] and Rakesh Chaudhari [1,*]

[1] Department of Mechanical Engineering, School of Technology, Pandit Deendayal Energy University, Raisan, Gandhinagar 382007, India; jay.vora@sot.pdpu.ac.in (J.V.); yug.smc18@sot.pdpu.ac.in (Y.S.); vivekp@sot.pdpu.ac.in (V.K.P.)
[2] School of Technology, Pandit Deendayal Energy University, Raisan, Gandhinagar 382007, India; sakshum.khanna@gmail.com
[3] Department of Mechanical Engineering, Vishwakarma Institute of Information Technology (An Autonomous Institute Affiliated to SPPU), Pune 411048, India; manoj.jagdale@viit.ac.in
* Correspondence: rakesh.chaudhari@sot.pdpu.ac.in

Abstract: Wire electrical discharge machining (WEDM) is widely preferred for machining difficult-to-cut materials like Ti6Al4V. In the present study, current, pulse-off-duration (T_{off}), and pulse-on-duration (T_{off}) were identified as vital input factors for the WEDM process of Ti6Al4V. Material removal rate (MRR) and surface roughness (SR) were selected as output measures for the study. The experiments were carried out by employing Taguchi's L9 design at three levels. Empirical models were generated, which give the relationship between the input and output factors of the process. To check the acceptability of the model terms, analysis of variance (ANOVA) was used. The regression mode was observed to be significant for the output measures. For MRR, Toff was recorded as the highly significant factor affecting the response values with 74.95% impact, followed by Ton with 16.39%, and current with 6.56%. In the case of SR, Ton was found to be a highly significant factor with a 50.24% impact, followed by current with 43.99%, and Toff with 1.47%. Further, multi-objective optimization by using the HTS technique was performed. The effect of expanded graphite (EG) nano-powder has been studied on the output factors of MRR and SR. The use of EG nano-powder was found to improve WEDM operations as MRR was increased by 45.35%, and simultaneously, SR was reduced by 36.16%. Lastly, the surface morphology of the machined surface was investigated by employing SEM to understand the effect of EG nano-powder. The results have shown a reduction in surface defects by using EG nano-powder compared to the conventional WEDM process.

Keywords: expanded graphite; Ti6Al4V; WEDM; HTS algorithm; nano-powder

Citation: Vora, J.; Shah, Y.; Khanna, S.; Patel, V.K.; Jagdale, M.; Chaudhari, R. Multi-Response Optimization and Influence of Expanded Graphite on Performance of WEDM Process of Ti6Al4V. *J. Manuf. Mater. Process.* **2023**, *7*, 111. https://doi.org/10.3390/jmmp7030111

Academic Editor: Muhammad Pervej Jahan

Received: 25 April 2023
Revised: 9 May 2023
Accepted: 30 May 2023
Published: 7 June 2023

1. Introduction

A highly favored titanium alloy, Ti6Al4V makes up more than half of all current titanium products. In the 1950s, Ti6Al4V alloy was initially created for various applications in the aerospace industry as it reduces the weight of heavily loaded constructions [1]. Ti6Al4V alloy is an ideal material for numerous aerospace components [2,3]. Ti6Al4V has a low mass ratio, superior bio-absorbability, good anti-corrosive properties, high endurance, and increased fracture resilience [4,5]. While the aerospace sector still prevails in the Ti6Al4V market, other application areas like the automotive, energy, maritime, and chemical-related sectors, load-bearing implants, fixing bone deformities, and other biomedical sectors have seen significant growth over the past 50 years [6–9]. However, Ti6Al4V poses many challenges during machining due to its high chemical reactivity with cutting tool materials and limited heat conductivity [10,11]. Conventional machining of Ti6Al4V is challenging owing to the poor thermal conductivity, increased temperature at the cutting edges, tool wear, improper chip shape, and poor tool life [12–14]. Thus, controlling the integrity of the surface caused by machining is still difficult today. Even though it

still takes time and money, choosing the right cutting conditions and tools can be done through an experimental campaign [15,16]. Due to these various difficulties of conventional techniques for Ti6Al4V alloy, different non-traditional procedures were employed [17,18]. One such non-traditional process widely preferred for machining difficult-to-cut materials such as Ti6Al4V is the wire electrical discharge machining (WEDM) process. In the WEDM process, the workpiece and wire electrode produce a sequence of discrete sparks that erode the material from the workpiece [19,20]. A thin layer of dielectric fluid is continuously delivered to the machining zone to flush away the eroded particles. Wire movement is numerically controlled to give the workpiece the appropriate three-dimensional shape and precision [21]. WEDM can be used to efficiently and inexpensively manufacture difficult-to-machine alloys, such as Ti6Al4V [22,23]. One can machine an element and get a desired output by changing various input process parameters. For a superior surface, WEDM requires managing several process factors [24–26]. Higher productivity is essential, along with better surface integrity. This can be attained by raising the material removal rate (MRR) while concurrently lowering the surface roughness (SR) value [27]. The selection of the ideal process parameters is crucial for sustainable production. The researchers primarily preferred Taguchi's experimental design due to the multiple advantages such as reduction in experimental trials and the relationship between input and output factors [28].

Devarasiddappa et al. [29] investigated the four process variables of the WEDM process by varying them at four distinct levels in an experimental analysis for SR of Ti6Al4V alloy. The primary aspect of their work was minimizing the SR of Ti6Al4V alloy. The results revealed that SR decreased by 2.65% at the optimal process parameters. Muhammad Umar Farooq et al. [30] machined convex and concave profiles in Ti6Al4V for this study using the WEDM process. Comprehensive research was done on the effects of four factors, which include servo voltage (V_s), wire feed, pulse-on-duration (T_{on}), and pulse-off-duration (T_{off}), on the geometrical accuracy of profiles, as well as the diameter of corners. The most essential parameters for influencing overcut in convex profile were discovered to be V_s and T_{off}. V_s, T_{on}, and T_{off} strongly influence corner radius control and undercut in the machining of concave profiles. Chaudhari et al. [31] used the WEDM process for the machining of Ti6Al4V alloy using Taguchi's L9 array. Their findings revealed that T_{on} had major control factors to affect MRR values while the current was a major significant factor for SR response. Lin et al. [32] highlighted the value of applying the grey-Taguchi approach to optimize several quality factors, including electrode depletion, MRR, and overcut, to enhance the Ti6Al4V alloy's micro-EDM finish quality. The experimental results show that the peak current and T_{on} are crucial factors in the micro-EDM of Ti6Al4V alloy. The utilization of Ti6Al4V alloy using EDM for different pulse parameters was investigated by Priyadarshini et al. [33]. MRR, SR, and TWR (tool wear rate) were selected as output factors. Using the Taguchi approach, an orthogonal array was found for the experiment. The best parametric settings were discovered using the hybrid grey relational-PCA-based Taguchi approach, which was compared with GRA-based Taguchi. The GRA-based PCA optimization process was found to produce more workable parametric settings. A large number of defects such as higher SR, debris deposition, significant dimensional deviations, the formation of micro-cracks and micro-pores, and lower productivity were found after machining [34,35].

It is crucial to find a way out which will improve MRR while reducing SR and other surface flaws. One efficient way to enhance machining is to add the right amount of nano-powder to the dielectric fluid [36,37]. The particle's presence in the dielectric fluid improves spark discharge, which lowers breakdown strength and improves the igniting process [38,39]. This enhances the process's ability to cut as a result. Researchers have employed a range of nano-powder, including Si, Cu, Al, CNT, Al_2O_3, Gr, Mo, and others, to enhance the machining operations [40]. Their effectiveness is influenced by variables like size, conductivity, and density characteristics [41]. The EDM's performance was significantly improved by the dispersion of nanoparticles in dielectric fluid [42,43]. Cutting

efficiency, SR, micro-cracks, and micro-pores were all enhanced when nanoparticles and dielectric fluid were used [44,45].

Viet De Bui et al. [46] conducted a study to provide additional evidence of powder-mixed EDM's capability in simultaneously cutting component shapes and coating a layer of antibacterial material on medical devices. In order to do this, varying silver nanoparticle concentrations were included in the dielectric, which was then utilized to machine Ti6Al4V. The surfaces machined and coated by the powder mixed EDM (PMEDM) approach showed a considerable reduction in the volume of the Staphylococcus bacteria and the number of bacterial groupings on the surface of the coating layer, according to qualitative as well as statistical measurements. The PMEDM method significantly reduces machining time compared to EDM without powder in terms of machining performance. Ishfaq et al. [47] examined the potential of nano-graphene from the standpoint of roughness in Ti-alloy EDM. The Taguchi L18 orthogonal framework, which incorporates six EDM parameters, was the foundation of the experimental design. With statistical analysis and tangible proof, the experimental results were thoroughly discussed. Compared to its rivals, an aluminum electrode produced the best surface quality; however, a brass electrode coupled with a graphene-mixed dielectric resulted in the worst surface asperities. Additionally, it is believed that for all types of electrodes, decreased roughness is provided by positive tool polarity. Chandra et al. [48] assessed the addition of YAG nanoparticle hybridized expandable graphite powder as a partial replacement of graphite in the refractory composition, the structural characteristics of Al_2O_3-MgO-C refractories. The experimental results demonstrated that, compared to refractories made with normal graphite compositions, those made with hybridized EG exhibited a significant improvement in structural characteristics.

Expanded graphite (EG), or exfoliated graphite, is a type of graphite material produced by subjecting natural or synthetic graphite to high temperatures and rapid heating in the presence of an intercalation agent such as sulfuric acid or a mixture of nitric and sulfuric acids [49]. This process causes the graphite to expand and separate into thin, flat flakes. The expanded graphite material has unique properties such as high thermal conductivity, good electrical conductivity, low density, and high chemical stability, making it useful in various applications such as thermal insulation, electrical conductors, fire retardants, and lubricants [50,51]. Additionally, expanded graphite can be further processed into various forms, such as sheets, foams, and powders, to suit specific applications. Thus, EG nano-powder can significantly enhance the WEDM operations owing to its potential for reinforcing and toughening structural ceramic composites.

In the present study, T_{on}, T_{off}, and current were identified as vital input factors for the WEDM process of Ti6Al4V, while MRR and SR were selected as output measures. Moreover, the effect of EG nano-powder has been studied on the machined surface's MRR, SR, and surface morphology. The experiments were carried out by employing Taguchi's L9 design. Empirical models were generated, which gave the relationship between the input and output factors of the process. To assess the acceptability of the model terms, ANOVA was used. Further, multi-objective optimization by using the heat transfer search (HTS) technique was performed. Lastly, the surface morphology of the machined surface was investigated by employing SEM to understand the effect of EG nano-powder.

2. Materials and Methods

2.1. Expanded Graphite Nano-Powder

Expanded graphite is a type of graphite material created by exposing natural or synthetic graphite to high temperatures and rapid heating in the presence of an intercalation agent, such as sulfuric acid or a mixture of nitric and sulfuric acid. The synthesis process of expanded graphite begins with the intercalation of graphite material with an intercalation agent. The intercalation process involved the insertion of molecules or ions into the spaces between the graphene layers of the graphite, causing the layers to separate slightly. The expanded graphite was synthesized using a chemical method, where natural graphite was treated with an oxidizing agent such as potassium permanganate, nitric acid, or hydrogen

peroxide. The oxidizing agent broke down the intercalated layers of graphite, causing the graphite to expand. The expanded graphite was then washed and dried to remove any residual chemicals. The obtained material is a highly porous, sponge-like material consisting of thin, flat flakes of loosely stacked graphite.

2.2. Experimental Set-Up and Conditions

The experiments were carried out by using Concord make DK7732 WEDM set-up. In the present work, molybdenum wire was preferred as the tool material with a diameter of 180 µm, and EDM oil was used as a dielectric fluid. Figure 1 displays an enlarged view of the employed experimental set-up. To investigate the effect of expanded graphite nano-powder, it was mixed with the dielectric fluid with a concentration of 1 g/L. The work material of Ti6Al4V was selected, with major elements of 6% of Al, 4% of V, and Ti as balance. A cylindrical rod of Ti6Al4V having 8 mm diameter was utilized for experimental trials. Based on the recent literature and outcomes of preliminary trials, T_{on}, T_{off}, and current were identified as vital input factors for the WEDM process, while MRR and SR were selected as output measures. The experiments were carried out by employing Taguchi's L9 design at three levels. Table 1 displays the conditions for input factors. Taguchi's approach has multiple advantages, reducing the experimental trial's relationship between input and output factors [52–54]. Thus, it has been adopted in the present work. Minitab software was used to generate empirical models showing the relationship between the process's input and output factors. To check the acceptability of the model terms, ANOVA was used.

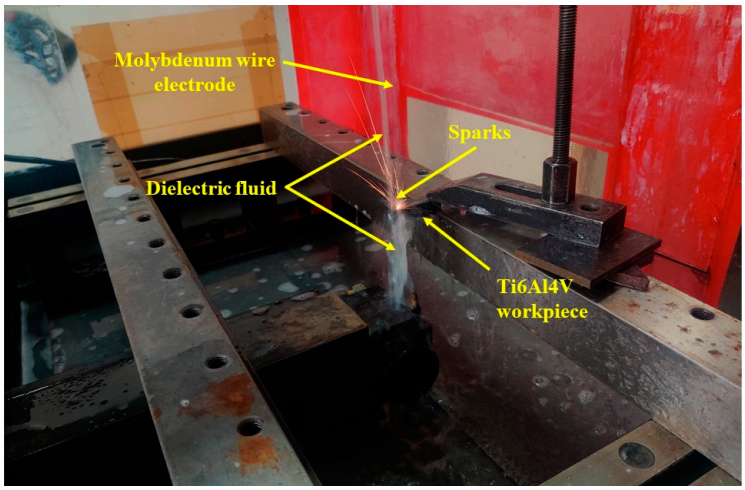

Figure 1. Enlarged view of experimental set-up.

Table 1. WEDM process factors.

Input Factors	Levels/Values
Current (A)	1, 3, 5
Pulse-off-duration (µs)	6, 16, 26
Pulse-on-duration (µs)	20, 60, 100
Type of nano-powder	Expanded Graphite
Graphene nano powder-size (nm)	200–400

For each experimental trial, a slice of 2 mm was cut by following the Taguchi's matrix and the time required for cut was recorded. The output measure of MRR was determined by evaluating the change in weights of work components before and after the process per second. The MRR response was recorded in gram/sec. The SR tester of Mitutoyo SJ-410 was employed to measure the SR of the machined components. In the current study, the arithmetic average-roughness (Ra) value (in µm) was considered for analysis. The

machined surface morphology was investigated by employing SEM to understand the effect of EG nano-powder.

2.3. Optimization

In the present study, the HTS algorithm proposed by Patel and Savsani [55], which functions on a heat transfer mechanism owing to the interface among the elements of a defined system and surrounding medium to attain equilibrium conditions, was implemented. It utilizes the three heat transfer modes—conduction, convection, and radiation—to attain an equilibrium condition. It creates an opportunity for all modes of heat transfer to exchange heat, and each generation selects a random mode out of the three modes. As a starting point, HTS operated with an arbitrarily produced population. The system defines the temperature level (i.e., design parameters) and population size. The population was then updated in subsequent generations by random selection of heat transfer mode. Finally, the solution which provides better functional values was acknowledged. The procedure for HTS is depicted in Figure 2.

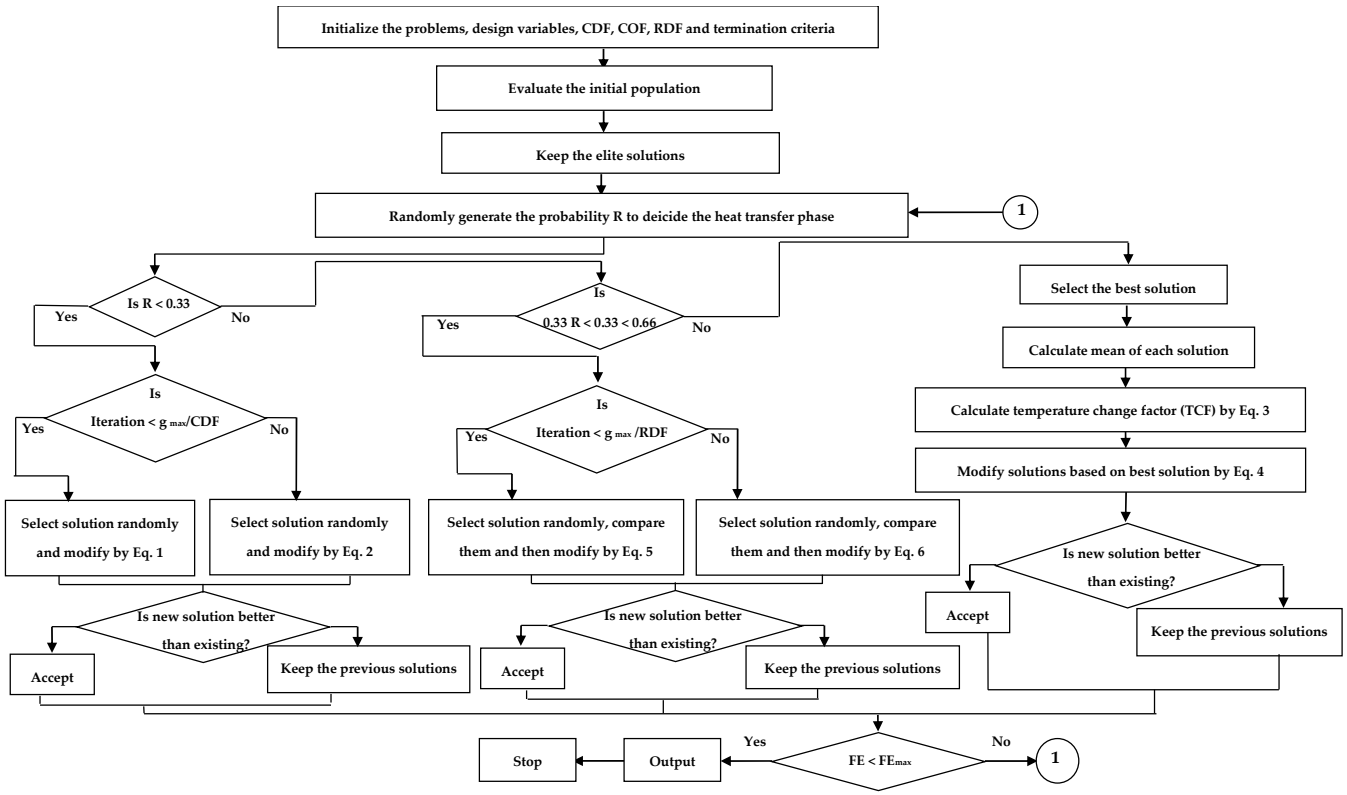

Figure 2. The procedure of HTS algorithm [55].

2.3.1. Conduction Mode

Equations (1) and (2) were utilized for improving the solutions from conduction mode.

$$X'_{j,i} = \begin{cases} X_{k,i} + \left(-R^2 X_{k,i}\right), \; if \; f\left(X_j\right) > f\left(X_k\right) \\ X_{j,i} + \left(-R^2 X_{j,i}\right), \; if \; f\left(X_j\right) < f\left(X_k\right) \end{cases} ; if \; g \leq {}^{g_{max}}/_{CDF} \tag{1}$$

$$X'_{j,i} = \begin{cases} X_{k,i} + \left(-r_i X_{k,i}\right), \; if \; f\left(X_j\right) > f\left(X_k\right) \\ X_{j,i} + \left(-r_i X_{j,i}\right), \; if \; f\left(X_j\right) < f\left(X_k\right) \end{cases} ; if \; g > {}^{g_{max}}/_{CDF} \tag{2}$$

2.3.2. Convection Mode

Equations (3) and (4) were utilized for improving the solutions from convection mode.

$$X'_{j,i} = X_{j,i} + R \times \left(X_s - X_{ms} \times TCF\right) \tag{3}$$

$$TCF = \begin{cases} abs(R - r_i),\ if\ g \leq {}^{g_{max}}/_{COF} \\ round(1 + r_i),\ if\ g > {}^{g_{max}}/_{COF} \end{cases} \quad (4)$$

2.3.3. Radiation Mode

Equations (5) and (6) were utilized for improving the solutions from conduction mode.

$$X'_{j,i} = \begin{cases} X_{j,i} + R \times (X_{k,i} - X_{j,i}),\ if\ f(X_j) > f(X_k) \\ X_{j,i} + R \times (X_{j,i} - X_{k,i}),\ if\ f(X_j) < f(X_k) \end{cases} ; if\ g \leq {}^{g_{max}}/_{RDF} \quad (5)$$

$$X'_{j,i} = \begin{cases} X_{j,i} + r_i \times (X_{k,i} - X_{j,i}),\ if\ f(X_j) > f(X_k) \\ X_{j,i} + r_i \times (X_{j,i} - X_{k,i}),\ if\ f(X_j) < f(X_k) \end{cases} ; if\ g > {}^{g_{max}}/_{RDF} \quad (6)$$

3. Results and Discussions

Table 2 depicts the derived values of MRR and SR output measures at the respective levels of input conditions by following Taguchi's L9 matrix. The value of MRR was obtained in the range of 1.1561 g/s to 3.3017 g/s, while SR response values were obtained between 3.32 µm to 5.72 µm.

Table 2. Results of MRR and SR as per Taguchi's L9 array.

Run Order	Current (A)	T_{off} (µs)	T_{on} (µs)	MRR (g/s)	SR (µm)
1	1	6	20	1.3741	4.89
2	1	16	60	1.8744	3.97
3	1	26	100	2.2235	3.32
4	3	6	60	2.6372	4.87
5	3	16	100	2.8013	4.66
6	3	26	20	1.1561	4.18
7	5	6	100	3.3017	5.72
8	5	16	20	1.5102	5.24
9	5	26	60	1.9287	4.49

3.1. Empirical Model Terms for Response Measures

The empirical regression equations were derived by using Minitab v17 for output factors. These equations are useful for measuring MRR and SR values outside the design matrix. Equations (7) and (8) depict the model terms for MRR and SR, respectively.

$$\text{MRR} = 1.236 + 0.10571 \cdot \text{Current} + 0.01786 \cdot T_{on} - 0.03341 \cdot T_{off} \quad (7)$$

$$\text{SR} = 4.857 + 0.2726 \cdot \text{Current} - 0.00250 \cdot T_{on} - 0.03341 \cdot T_{off} \quad (8)$$

3.2. ANOVA Analysis for Response Measures

ANOVA methodology was implemented to evaluate the adequacy of the generated equations. The 95% CI was used to ensure the effect of the model terms. During this, a *p*-value lower than 0.05 implies that the corresponding term has some effect on the specified output measure [56,57].

3.2.1. MRR

Table 3 shows the ANOVA results at a 95% CI for the regression equations generated among the investigated factors and MRR. The regression model term considerably impacted the created model terms for all of the examined metrics. The results revealed that the entire regression terms, including all input parameters, significantly affect MRR response. As per the obtained results, MRR was highly dependent on T_{off}. T_{off} contributes the most (74.95%) to MRR, followed by T_{on} (16.39%) and current (6.56%). The R^2 value of 97.92% implies that the empirical model can explain 97.92% of the variation in MRR, whereas the

created model cannot explain just 2.08% of the entire variation. When the expected and adjusted R^2 values concur, it confirms a significant connection between the observed and anticipated values [58]. In this case, adjusted R^2 was 96.67% and anticipated R^2 was 93.18%. The close proximity of the values indicates a strong relationship between them. This clearly demonstrates the model's acceptability and sufficiency.

Table 3. ANOVA for MRR.

Source	Adj. SS	F-Value	*p*-Value	% Contribution
Regression	3.9998	78.46	0.000	
Current	0.2682	15.78	0.011	6.56
T_{off}	3.0618	180.18	0.000	74.95
T_{on}	0.6698	39.42	0.002	16.39
Error	0.0849			2.10
Total	4.0848			100
R^2 = 97.92%, R^2 adj. = 96.67%, R^2 pred. = 93.18%				

3.2.2. SR

Table 4 shows the ANOVA results for SR. The regression model term has considerably impacted the created model terms for all of the examined metrics. The results revealed that the entire regression terms, including input parameters of T_{on} and current, significantly affect the SR response. T_{off} did not have a significant effect on SR response. As per the obtained results, SR was highly dependent on T_{on}. T_{on} contributes the most (50.24%) to SR, followed by current (43.99%) and T_{off} (1.47%). The R^2 value of 95.72% implies that the empirical model can explain 95.72% of the variation in SR whereas the created model cannot explain just 4.28% of the entire variation. When the expected and adjusted R^2 values concur, it confirms a significant connection between the observed and anticipated values [59]. In this case, the adjusted R^2 is 93.15% and the anticipated R^2 is 87.2%. The close proximity of the values indicates a strong relationship between them. This clearly demonstrates the model's acceptability and sufficiency.

Table 4. ANOVA for SR.

Source	Adj. SS	F-Value	*p*-Value	% Contribution
Regression	3.8792	37.28	0.001	
Current	1.7831	51.41	0.001	43.99
T_{off}	0.0599	1.73	0.246	1.47
T_{on}	2.0363	58.71	0.001	50.24
Error	0.1734			4.30
Total	4.0526			100
R^2 = 95.72%, R^2 adj. = 93.15%, R^2 pred. = 87.20%				

3.3. Residual Plots for MRR and SR Measures

The positive findings of the ANOVA results are supported by residual plots. If certain conditions are met, ANOVA analysis might be regarded as valid and acceptable for the chosen model [60]. For this aim, residual plot validation is critical. Figure 3 shows the residual plot for MRR. The normality plot depicts linear progression. It means that the model is suitable. The second vs fit graph indicated that fits around the source was absolutely random. A bell-shaped curve represents the data required for a powerful ANOVA in the histogram display [61]. The Versus order plot confirms the ANOVA results, which revealed no discernible trend. The four residual plots in the current investigation verified the ANOVA statistics for a more accurate results forecast.

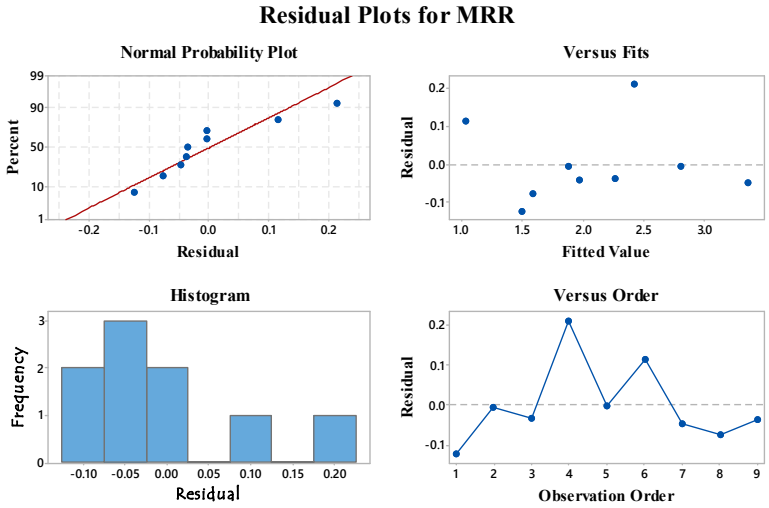

Figure 3. Residual plots for MRR.

The SR readings for all four residuals were similar to MRR, as shown in Figure 4. Thus, the residual plot findings for all performance metrics imply good ANOVA results and satisfy the ANOVA requirement.

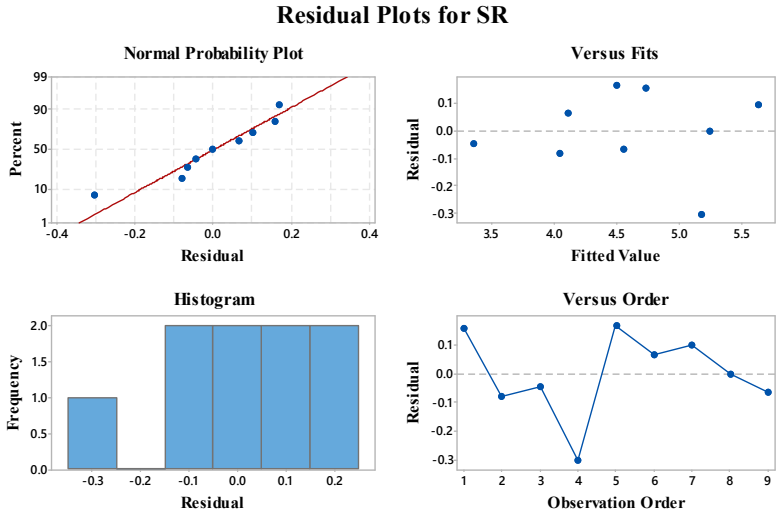

Figure 4. Residual plots for SR.

3.4. Main Effect Plots for Response Measures

3.4.1. Main Effect Plot for MRR

Figure 5 demonstrates the effect of WEDM factors on the MRR output measure. The *X*-axis indicated WEDM variables, while the *Y*-axis depicted MRR means for the relevant input. It was discovered that as the current increased, so did the MRR. This is due to a spike in discharge energy caused by the current value. The subsequent rise in heat energy melts and vaporizes the work material, resulting in a surge in thermal energy produced by growth in discharge energy [34,62]. When additional melting and vaporization occurs, more work material erodes at the machining zone, enhancing the MRR value. An increase in T_{off} value led to a reduction in the value of MRR in the T_{off} vs. MRR plot. When the T_{off} value is increased, the discharge energy decreases. As T_{off} increases, spark amplitude and discharge energy decline, as does MRR, because MRR is directly correlated to discharge energy [40]. In the case of T_{on} vs. MRR, it was discovered that as the value of T_{on} increased, so did the value of MRR. The material erodes as a result of the machining process's use of a repeating spark. These discharges grow as the T_{on} increases. The workpiece melted

and vaporized as the heat energy was raised. Higher melting and vaporization cause more erosion of the work materials, resulting in an increase in MRR [63]. Setting current and T_{on} at higher levels and T_{off} at a lower level is optimal for increasing MRR.

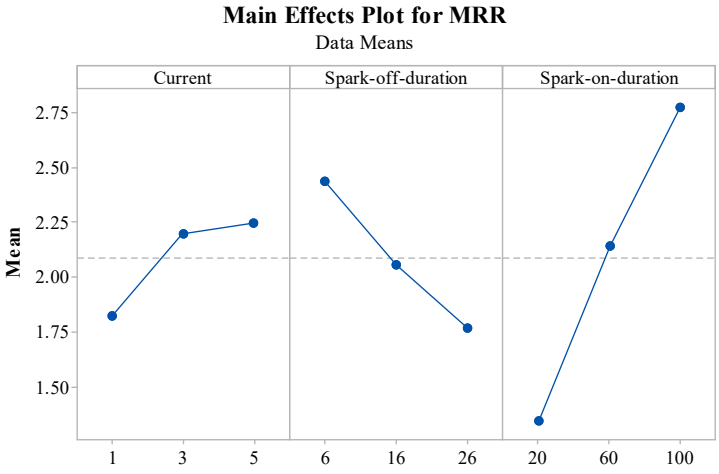

Figure 5. Main effect plot for MRR.

3.4.2. Main Effect Plot for SR

The graph shown in Figure 6 depicts the effect of WEDM factors on SR output measurements. The *X*-axis displays WEDM variables and the *Y*-axis displays the means of the SR measure for each input. The major effect plot for current vs. SR revealed that as the current increases, so does the SR. The higher value causes enlarged discharge energy, which causes a rise in heat energy. Thus, the material gets melted and vaporized owing to this heat energy. These increases in thermal energy and sparks result in higher temperatures, which raises the SR [64]. When the rate of erosion increases due to an increase in current, large and deep craters formed on the work material produce a more even surface. With an increase in T_{off} value, SR value decreased. T_{off} was found to affect SR when it was increased favorably. A decrease in spark intensity decreases the temperature further as T_{off} rises. As T_{off} increases, reducing thermal and discharge energy. This formed a small crater and improved the surface smoothness of the material being machined [65]. As a result, as T_{off} rises, SR falls. With an increase T_{on}, SR was initially decreased and then slightly increased. This was because, at the higher T_{on}, a large amount of metal was deposited on machined parts as it does not have sufficient time to flush away due to a higher amount of discharge energy [28].

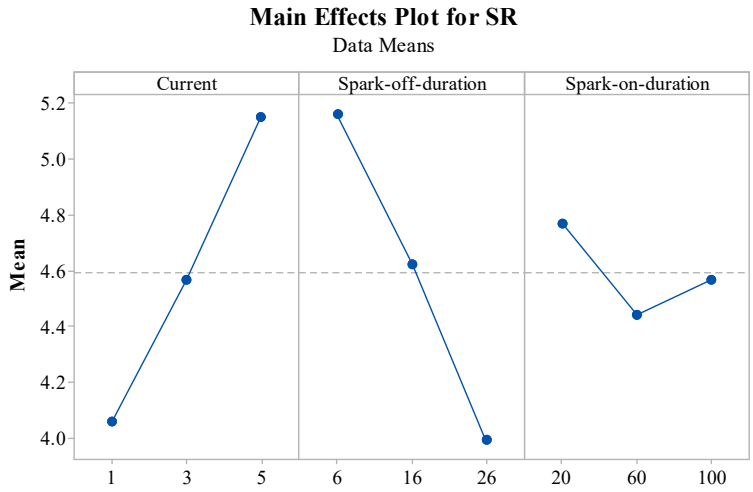

Figure 6. Main effect plot for SR.

3.5. Optimization Results

The results of ANOVA and the main effect plots clearly depict the need to optimize process parameters, as it has shown conflicting conditions of input factors for MRR and SR responses. Thus, the current study has employed the HTS algorithm by considering the upper and lower bounds of the input factors employed for Taguchi's design.

Initially, a single-response optimization was carried out for MRR and SR. MRR was referred to as the maximization criterion for higher productivity, while SR was considered a minimization function to acquire a better surface finish. The obtained results of single-response optimization are depicted in Table 5. A conflicting situation can be clearly observed in the results and input factor conditions. This can be efficiently handled by simultaneous optimization of multiple responses. Pursuant to this, non-dominated solutions were obtained by generating the Pareto points through a multi-objective HTS algorithm.

Table 5. Results of single-response optimization.

Function	Input Factors			Output Measures	
	Current (A)	T_{off} (µs)	T_{on} (µs)	MRR (g/s)	SR (µm)
Maximum MRR	5	6	100	3.3501	5.62
Minimum SR	1	26	100	2.2590	3.36

Figure 7 depicts a 2D Pareto graph of the obtained Pareto points by implementing the MOHTS technique. These points are also represented in Table 6, along with their input factors. Pareto points were achieved after using multiple evaluation functions. All the obtained results of Pareto points depict a unique solution that provides a trade-off among the conflicting responses. The MRR vs. SR plot, as shown in Figure 7, clearly depicts a contradictory nature among the response variables. Thus, a user can select the machining conditions as per their required levels of response values. Validation of the obtained results from the HTS algorithm was carried out by performing actual experimental trials. The predicted and actual results from the trial have shown an acceptable difference between their values. Thus, the HTS algorithm clearly suggested a wide acceptability for the developed models of the current work.

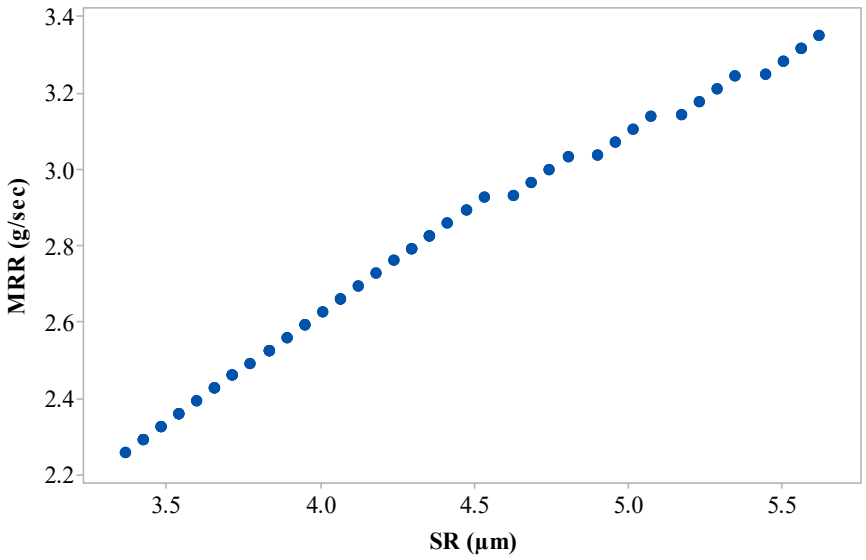

Figure 7. 2D Pareto graph for output measures.

Table 6. Predicted results of HTS algorithm.

Sr. No.	Current (A)	T_{off} (μs)	T_{on} (μs)	MRR (g/s)	SR (μm)
1	5	6	100	3.3501	5.62
2	1	26	100	2.2590	3.36
3	5	8	100	3.2832	5.50
4	1	13	100	2.6934	4.12
5	3	7	100	3.1052	5.02
6	1	12	100	2.7268	4.18
7	3	8	100	3.0718	4.96
8	2	7	100	2.9995	4.74
9	1	7	100	2.8938	4.47
10	5	9	100	3.2498	5.45
11	3	9	100	3.0384	4.90
12	1	6	100	2.9272	4.53
13	2	9	100	2.9327	4.63
14	4	6	100	3.2443	5.35
15	2	6	100	3.0329	4.80
16	4	9	100	3.1441	5.17
17	3	6	100	3.1386	5.08
18	1	19	100	2.4929	3.77
19	1	24	100	2.3259	3.48
20	1	18	100	2.5263	3.83
21	1	11	100	2.7602	4.24
22	1	23	100	2.3593	3.54
23	1	10	100	2.7936	4.30
24	2	8	100	2.9661	4.69
25	4	8	100	3.1775	5.23
26	1	8	100	2.8604	4.41
27	1	14	100	2.6600	4.06
28	1	9	100	2.8270	4.36
29	1	17	100	2.5597	3.89
30	1	23	100	2.3593	3.54
31	1	15	100	2.6266	4.01
32	1	20	100	2.4595	3.71
33	1	24	100	2.3259	3.48
34	1	25	100	2.2925	3.42
35	1	21	100	2.4261	3.66
36	1	20	100	2.4595	3.71
37	1	16	100	2.5931	3.95
38	1	22	100	2.3927	3.60
39	1	18	100	2.5263	3.83
40	1	10	100	2.7936	4.30
41	1	9	100	2.8270	4.36
42	1	14	100	2.6600	4.06
43	1	25	100	2.2925	3.42
44	1	16	100	2.5931	3.95
45	1	21	100	2.4261	3.66
46	5	7	100	3.3166	5.56
47	4	7	100	3.2109	5.29
48	5	7	100	3.3166	5.56

3.6. Effect of Expanded Graphite on Output Factors

The effect of expanded graphite (EG) nano-powder has been studied on the output factors of MRR and SR. To understand the effect of EG, an objective function was used (Equation (9)) by assigning equal weightage to both responses.

$$\text{Obj.} = w_1 \cdot (\text{MRR}) + w_2 \cdot (\text{SR}) \quad (9)$$

As per the above objective function, experiments were conducted with and without the use of EG nano-powder, as shown in Table 7. An equal weightage of 0.5 was given to MRR and SR. The objective function has input factor conditions of T_{on} at 100 µs, T_{off} at 13 µs, and current at 1 A. Thus, the experiment was carried out with these input factors. As seen from Table 7, the obtained values of MRR and SR at conventional WEDM conditions, i.e., without the use of EG, were 2.69 g/s and 4.12 µm, respectively. In contrast, the use of EG nano-powder at 1 g/L has shown enhancement in response values with MRR of 3.91 g/s and SR of 2.623 µm. This has shown an enhancement of 45.35% and 36.16% for MRR and SR, respectively. This was due to the fact that the addition of EG in the dielectric fluid has improved spark discharge, which lowers breakdown strength and improves the igniting process [37,66]. In addition to this, the addition of EG helps in flushing the eroded particles.

Table 7. Impact of expanded graphite.

Experimental Condition	WEDM Factors	Response Measures
Use of Expanded Graphite nano-powder	Current = 1 A T_{on} = 100 µs T_{off} = 13 µs EG nano-powder = 1 g/L	MRR = 3.91 g/s SR = 2.63 µm
Without EG nano-powder (Conventional EDM)	Current = 1 A T_{on} = 100 µs T_{off} = 13 µs EG nano-powder = 1 g/L	MRR = 2.69 g/s SR = 4.12 µm

3.7. Effect of Expanded Graphite on Surface Morphology

The surface morphology of the machined surface was investigated by employing SEM to understand the effect of EG nano-powder. The optimum corresponding process parameters shown in Table 7 were used in this study to investigate the surface anatomy of machined surfaces of conventional WEDM (T_{on} at 100 µs, T_{off} at 13 µs, and current at 1 A, and without EG nano-powder) and PMWEDM (T_{on} at 100 µs, T_{off} at 13 µs, and current at 1 A, and EG nano-powder conc. at 1 g/L) processes. Figures 8 and 9 show micrographs obtained from SEM of the machined area during traditional WEDM and PMWEDM processes. Analyzing the surface obtained in Figure 8 reveals an extensive number of micro-pores, increased layer deposition, i.e., the development of globules and the existence of micro-cracks. However, the machined surface of PMWEDM obtained using the same machining parameters as the standard WEDM method exhibited a significant improvement in surface defects, i.e., a significant reduction in micro-pores, globules, and micro-cracks. The consistent sparking between the work material and the tool reduces microcracks significantly in the PMWEDM process [67,68]. The significant gap between the tool and the workpiece is the cause of the large reduction in deposition of debris (globules) and micro-pores in the NPMWEDM process [69]. This results in suitable and simple debris flushing. This simple removal of dirt creates little ridges, which improves surface quality.

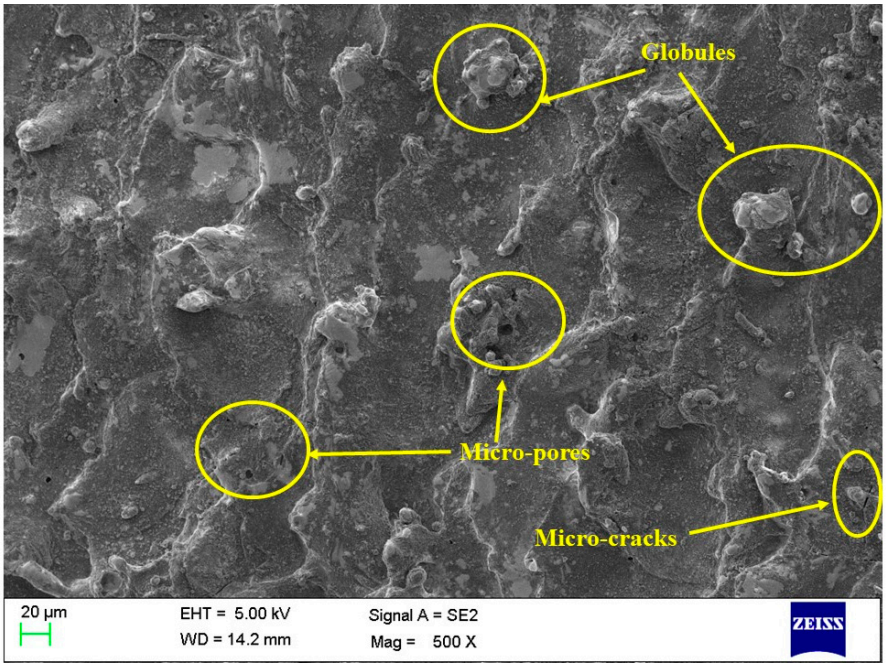

Figure 8. SEM image for conventional WEDM.

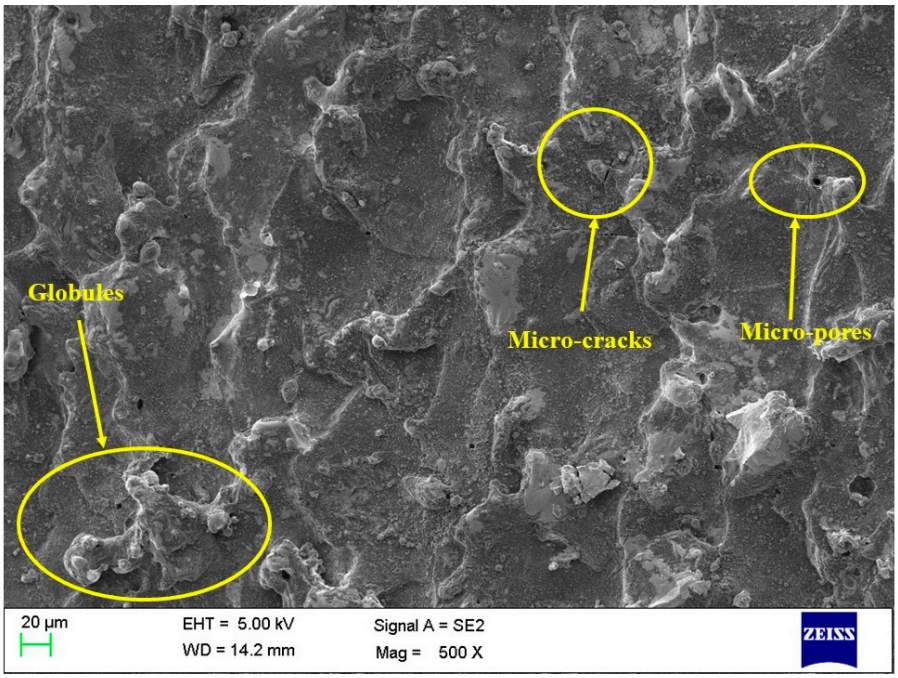

Figure 9. SEM image for EG nano-powder mixed with WEDM.

4. Conclusions

In the present work, the effect of EG nano-powder has been studied on MRR, SR, and surface morphology of the machined surfaces. Current, T_{on}, and T_{off} were identified as vital input factors for the WEDM process of Ti6Al4V. The experiments were carried out by employing Taguchi's L9 design. The empirical regression equations were derived by using Minitab v17 for output factors. The regression mode was observed to be significant for the output measures. ANOVA was used to assess the acceptability of the suggested regression equations. For MRR, T_{off} was recorded to be the most important factor affecting the response values with 74.95% impact, followed by T_{on} with 16.39% and current with

6.56%. In the case of SR, T_{on} was found to be a highly significant factor with a 50.24% impact, followed by current with 43.99%, and T_{off} with 1.47%. The regression values close to 100 confirmed the results' suitability. Additionally, residual plots for both responses also verified the successful outcome. An HTS algorithm was implemented for single-response and multi-response optimization. The results of single-response optimization have shown a conflicting situation in response parameters. Pursuant to this, non-dominated solutions were obtained by generating the Pareto points through a multi-objective HTS algorithm. The effect of expanded graphite (EG) nano-powder has been studied on the output factors of MRR and SR. The MRR and SR at conventional EDM conditions, i.e., without using EG, were recorded as 2.69 g/s and 4.12 μm, respectively. In contrast, the use of EG nano-powder at 1 g/L has shown enhancement in response values with MRR of 3.91 g/s and SR of 2.623 μm. This has shown an enhancement of 45.35% and 36.16% for MRR and SR, respectively. Lastly, the surface morphology of the machined surface was investigated by employing SEM to understand the effect of EG nano-powder. The results showed a reduction in surface defects when using EG nano-powder compared to the conventional WEDM process.

Author Contributions: Conceptualization, R.C. and J.V.; methodology, R.C., M.J. and Y.S.; software, V.K.P., M.J. and S.K.; validation, R.C., J.V. and Y.S.; formal analysis, R.C.; investigation, R.C., J.V., M.J., Y.S., V.K.P. and S.K.; data curation, R.C.; writing—original draft preparation, Y.S. and R.C.; writing—review and editing, J.V., V.K.P. and S.K.; visualization, R.C. and S.K.; supervision, R.C. All authors have read and agreed to the published version of the manuscript.

Funding: This research received no external funding.

Data Availability Statement: Data presented in this study are available in this article.

Conflicts of Interest: The authors declare no conflict of interest.

Nomenclature

ANOVA	Analysis of variance
CI	Confidence interval
DOE	Design of experiments
EDM	Electrical discharge machining
EG	Expanded graphite
HTS	Heat transfer search
MOHTS	Multi-objective heat transfer search
MRR	Material removal rate (g/s)
PMEDM	Powder-mixed electrical discharge machining
PMWEDM	Powder-mixed wire electrical discharge machining
SEM	Scanning electron microscope
SR	Surface roughness (μm)
T_{on}	Pulse on time (μs)
T_{off}	Pulse off time (μs)
t	Time in seconds
RLT	Recast layer thickness
WEDM	Wire electric discharge machine
ρ	Density in g/cm^3
R	Probability
n	Randomy generated initial population
g	Updated population in each generation
m	Number of optimization parameters
i	1, 2, . . . , m
j	1, 2, . . . , n
k	Randomy selection solution from population
$X_{j,i}$, $X_{k,i,}$ . . .	Temperature gradients
CDF	Conduction factor
COF	Convection factor
RDF	Radiation factor

References

1. Wanjara, P.; Backman, D.; Sikan, F.; Gholipour, J.; Amos, R.; Patnaik, P.; Brochu, M. Microstructure and mechanical properties of Ti-6Al-4V additively manufactured by electron beam melting with 3D part nesting and powder reuse influences. *J. Manuf. Mater. Process.* **2022**, *6*, 21. [CrossRef]
2. Boyer, R.R. An overview on the use of titanium in the aerospace industry. *Mater. Sci. Eng. A* **1996**, *213*, 103–114. [CrossRef]
3. Outeiro, J.; Cheng, W.; Chinesta, F.; Ammar, A. Modelling and optimization of machining of Ti-6Al-4V titanium alloy using machine learning and design of experiments methods. *J. Manuf. Mater. Process.* **2022**, *6*, 58. [CrossRef]
4. Cui, C.; Hu, B.; Zhao, L.; Liu, S. Titanium alloy production technology, market prospects and industry development. *Mater. Des.* **2011**, *32*, 1684–1691. [CrossRef]
5. Chaudhari, R.; Vora, J.; Parikh, D.; Wankhede, V.; Khanna, S. Multi-response optimization of WEDM parameters using an integrated approach of RSM–GRA analysis for pure titanium. *J. Inst. Eng. Ser. D* **2020**, *101*, 117–126. [CrossRef]
6. Farshid, S.; Ebrahimian-Hosseinabadi, M.; Rafienia, M. Electrophoretic deposition of biphasic calcium phosphate/graphene nanocomposite coatings on Ti6Al4V substrate for biomedical applications. *J. Alloy. Compd.* **2022**, *892*, 162150. [CrossRef]
7. Kugalur Palanisamy, N.; Rivière Lorphèvre, E.; Gobert, M.; Briffoteaux, G.; Tuyttens, D.; Arrazola, P.-J.; Ducobu, F. Identification of the Parameter Values of the Constitutive and Friction Models in Machining Using EGO Algorithm: Application to Ti6Al4V. *Metals* **2022**, *12*, 976. [CrossRef]
8. Fuse, K.; Chaudhari, R.; Vora, J.; Patel, V.K.; de Lacalle, L.N.L. Multi-Response Optimization of Abrasive Waterjet Machining of Ti6Al4V Using Integrated Approach of Utilized Heat Transfer Search Algorithm and RSM. *Materials* **2021**, *14*, 7746. [CrossRef]
9. Rajput, G.S.; Vora, J.; Prajapati, P.; Chaudhari, R. Areas of recent developments for shape memory alloy: A review. *Mater. Today Proc.* **2022**, *62*, 7194–7198. [CrossRef]
10. Vora, J.; Chaudhari, R.; Patel, C.; Pimenov, D.Y.; Patel, V.K.; Giasin, K.; Sharma, S. Experimental investigations and Pareto optimization of fiber laser cutting process of Ti6Al4V. *Metals* **2021**, *11*, 1461. [CrossRef]
11. Pradhan, S.; Singh, S.; Prakash, C.; Królczyk, G.; Pramanik, A.; Pruncu, C.I. Investigation of machining characteristics of hard-to-machine Ti-6Al-4V-ELI alloy for biomedical applications. *J. Mater. Res. Technol.* **2019**, *8*, 4849–4862. [CrossRef]
12. Fuse, K.; Dalsaniya, A.; Modi, D.; Vora, J.; Pimenov, D.Y.; Giasin, K.; Prajapati, P.; Chaudhari, R.; Wojciechowski, S. Integration of fuzzy AHP and fuzzy TOPSIS methods for wire electric discharge machining of titanium (Ti6Al4V) alloy using RSM. *Materials* **2021**, *14*, 7408. [CrossRef] [PubMed]
13. Sarıkaya, M.; Gupta, M.K.; Tomaz, I.; Pimenov, D.Y.; Kuntoğlu, M.; Khanna, N.; Yıldırım, Ç.V.; Krolczyk, G.M. A state-of-the-art review on tool wear and surface integrity characteristics in machining of superalloys. *CIRP J. Manuf. Sci. Technol.* **2021**, *35*, 624–658. [CrossRef]
14. Hourmand, M.; Sarhan, A.A.; Sayuti, M.; Hamdi, M. A comprehensive review on machining of titanium alloys. *Arab. J. Sci. Eng.* **2021**, *46*, 7087–7123. [CrossRef]
15. Khanna, N.; Zadafiya, K.; Patel, T.; Kaynak, Y.; Rashid, R.A.R.; Vafadar, A. Review on machining of additively manufactured nickel and titanium alloys. *J. Mater. Res. Technol.* **2021**, *15*, 3192–3221. [CrossRef]
16. Vora, J.; Jain, A.; Sheth, M.; Gajjar, K.; Abhishek, K.; Chaudhari, R. A review on machining aspects of shape memory alloys. In *Recent Advances in Mechanical Infrastructure*; Springer: Singapore, 2022; pp. 449–458.
17. Sethy, S.; Behera, R.K.; Davim, J.P.; Rana, J. Effect of Thermo-Physical Properties of the Tool Materials on the Electro-Discharge Machining Performance of Ti-6Al-4V and SS316 Work Piece Materials. *J. Manuf. Mater. Process.* **2022**, *6*, 96. [CrossRef]
18. Dekster, L.; Karkalos, N.E.; Karmiris-Obratański, P.; Markopoulos, A.P. Evaluation of the Machinability of Ti-6Al-4V Titanium Alloy by AWJM Using a Multipass Strategy. *Appl. Sci.* **2023**, *13*, 3774. [CrossRef]
19. Rathi, P.; Ghiya, R.; Shah, H.; Srivastava, P.; Patel, S.; Chaudhari, R.; Vora, J. Multi-response optimization of Ni55. 8Ti shape memory alloy using taguchi–grey relational analysis approach. In *Recent Advances in Mechanical Infrastructure: Proceedings of the ICRAM 2019, Ahmedabad, India, 20–21 April 2019*; Springer: Singapore, 2019; pp. 13–23.
20. Chaudhari, R.; Ayesta, I.; Doshi, M.; Khanna, S.; Patel, V.K.; Vora, J.; De Lacalle, L.N.L. Effect of Multi-walled carbon nanotubes on the performance evaluation of Nickel-based super-alloy–Udimet 720 machined using WEDM process. *Int. J. Adv. Manuf. Technol.* **2022**, *123*, 2087–2105. [CrossRef]
21. Chaudhari, R.; Shah, H.; Ayesta, I.; de Lacalle, L.L.; Vora, J. Experimental investigations and optimization of WEDM parameters using Taguchi analysis of pure titanium. In *Recent Advances in Mechanical Infrastructure: Proceedings of the ICRAM 2021*; Springer: Singapore, 2022; pp. 349–358.
22. Sharma, N.; Gupta, R.D.; Khanna, R.; Sharma, R.C.; Sharma, Y.K. Machining of Ti-6Al-4V biomedical alloy by WEDM: Investigation and optimization of MRR and Rz using grey-harmony search. *World J. Eng.* **2023**, *20*, 221–234. [CrossRef]
23. Maurya, R.; Porwal, R.K.; Singh, R. Concerning drifts to optimization techniques of wire-EDM process for titanium based super alloys: A review. *Mater. Today Proc.* **2019**, *18*, 4509–4514. [CrossRef]
24. Chaudhari, R.; Vora, J.J.; Mani Prabu, S.; Palani, I.; Patel, V.K.; Parikh, D.; de Lacalle, L.N.L. Multi-response optimization of WEDM process parameters for machining of superelastic nitinol shape-memory alloy using a heat-transfer search algorithm. *Materials* **2019**, *12*, 1277. [CrossRef]
25. Chaudhari, R.; Vora, J.J.; Prabu, S.M.; Palani, I.; Patel, V.K.; Parikh, D. Pareto optimization of WEDM process parameters for machining a NiTi shape memory alloy using a combined approach of RSM and heat transfer search algorithm. *Adv. Manuf.* **2021**, *9*, 64–80. [CrossRef]

26. Vakharia, V.; Vora, J.; Khanna, S.; Chaudhari, R.; Shah, M.; Pimenov, D.Y.; Giasin, K.; Prajapati, P.; Wojciechowski, S. Experimental investigations and prediction of WEDMed surface of Nitinol SMA using SinGAN and DenseNet deep learning model. *J. Mater. Res. Technol.* **2022**, *18*, 325–337. [CrossRef]
27. Gupta, A.; Kumar, H. Optimization of EDM process parameters: A review of technique, process, and outcome. In *Advances in Manufacturing Industrial Engineering*; Springer: Singapore, 2021; pp. 981–996.
28. Chaudhari, R.; Vora, J.J.; Pramanik, A.; Parikh, D. Optimization of parameters of spark erosion based processes. In *Spark Erosion Machining*; CRC Press: Boca Raton, FL, USA, 2020; pp. 190–216.
29. Devarasiddappa, D.; Chandrasekaran, M.; Arunachalam, R. Experimental investigation and parametric optimization for minimizing surface roughness during WEDM of Ti6Al4V alloy using modified TLBO algorithm. *J. Braz. Soc. Mech. Sci. Eng.* **2020**, *42*, 128. [CrossRef]
30. Farooq, M.U.; Ali, M.A.; He, Y.; Khan, A.M.; Pruncu, C.I.; Kashif, M.; Ahmed, N.; Asif, N. Curved profiles machining of Ti6Al4V alloy through WEDM: Investigations on geometrical errors. *J. Mater. Res. Technol.* **2020**, *9*, 16186–16201. [CrossRef]
31. Vora, J.; Prajapati, N.; Patel, S.; Sheth, S.; Patel, A.; Khanna, S.; Ayesta, I.; de Lacalle, L.L.; Chaudhari, R. Multi-response optimization and effect of alumina mixed with dielectric fluid on WEDM process of Ti6Al4V. In *Recent Advances in Mechanical Infrastructure: Proceedings of the ICRAM 2021*; Springer: Singapore, 2022; pp. 277–287.
32. Lin, M.; Tsao, C.; Huang, H.; Wu, C.; Hsu, C. Use of the grey-Taguchi method to optimise the micro-electrical discharge machining (micro-EDM) of Ti-6Al-4V alloy. *Int. J. Comput. Integr. Manuf.* **2015**, *28*, 569–576. [CrossRef]
33. Priyadarshini, M.; Pal, K. Multi-objective optimisation of EDM process using hybrid Taguchi-based methodologies for Ti-6Al-4V alloy. *Int. J. Manuf. Res.* **2016**, *11*, 144–166. [CrossRef]
34. Alam, M.N.; Siddiquee, A.N.; Khan, Z.A.; Khan, N.Z. A comprehensive review on wire EDM performance evaluation. *Proc. Inst. Mech. Eng. Part E J. Process Mech. Eng.* **2022**, *236*, 1724–1746. [CrossRef]
35. Mao, X.; Almeida, S.; Mo, J.; Ding, S. The state of the art of electrical discharge drilling: A review. *Int. J. Adv. Manuf. Technol.* **2022**, *121*, 2947–2969. [CrossRef]
36. Kumar, S.S.; Varol, T.; Canakci, A.; Kumaran, S.T.; Uthayakumar, M. A review on the performance of the materials by surface modification through EDM. *Int. J. Lightweight Mater. Manuf.* **2021**, *4*, 127–144. [CrossRef]
37. Abdudeen, A.; Abu Qudeiri, J.E.; Kareem, A.; Ahammed, T.; Ziout, A. Recent advances and perceptive insights into powder-mixed dielectric fluid of EDM. *Micromachines* **2020**, *11*, 754. [CrossRef] [PubMed]
38. Chaudhari, R.; Khanna, S.; Vora, J.; Patel, V.K.; Paneliya, S.; Pimenov, D.Y.; Giasin, K.; Wojciechowski, S. Experimental investigations and optimization of MWCNTs-mixed WEDM process parameters of nitinol shape memory alloy. *J. Mater. Res. Technol.* **2021**, *15*, 2152–2169. [CrossRef]
39. Chaudhari, R.; Prajapati, P.; Khanna, S.; Vora, J.; Patel, V.K.; Pimenov, D.Y.; Giasin, K. Multi-response optimization of Al_2O_3 nanopowder-mixed wire electrical discharge machining process parameters of nitinol shape memory alloy. *Materials* **2022**, *15*, 2018. [CrossRef] [PubMed]
40. Al-Amin, M.; Abdul Rani, A.M.; Abdu Aliyu, A.A.; Abdul Razak, M.A.H.; Hastuty, S.; Bryant, M.G. Powder mixed-EDM for potential biomedical applications: A critical review. *Mater. Manuf. Process.* **2020**, *35*, 1789–1811. [CrossRef]
41. Vora, J.; Khanna, S.; Chaudhari, R.; Patel, V.K.; Paneliya, S.; Pimenov, D.Y.; Giasin, K.; Prakash, C. Machining parameter optimization and experimental investigations of nano-graphene mixed electrical discharge machining of nitinol shape memory alloy. *J. Mater. Res. Technol.* **2022**, *19*, 653–668. [CrossRef]
42. Alhodaib, A.; Shandilya, P.; Rouniyar, A.K.; Bisaria, H. Experimental investigation on silicon powder mixed-EDM of nimonic-90 superalloy. *Metals* **2021**, *11*, 1673. [CrossRef]
43. Joshi, A.Y.; Joshi, A.Y. A systematic review on powder mixed electrical discharge machining. *Heliyon* **2019**, *5*, e02963. [CrossRef]
44. Kiran, P.; Mohanty, S.; Das, A.K. Surface modification through sustainable micro-EDM process using powder mixed bio-dielectrics. *Mater. Manuf. Process.* **2022**, *37*, 640–651. [CrossRef]
45. Singh, S.; Patel, B.; Upadhyay, R.K.; Singh, N.K. Improvement of process performance of powder mixed electrical discharge machining by optimisation-A Review. *Adv. Mater. Process. Technol.* **2022**, *8*, 3074–3104. [CrossRef]
46. Bui, V.D.; Mwangi, J.W.; Meinshausen, A.-K.; Mueller, A.J.; Bertrand, J.; Schubert, A. Antibacterial coating of Ti-6Al-4V surfaces using silver nano-powder mixed electrical discharge machining. *Surf. Coat. Technol.* **2020**, *383*, 125254. [CrossRef]
47. Ishfaq, K.; Maqsood, M.A.; Anwar, S.; Harris, M.; Alfaify, A.; Zia, A.W. EDM of Ti6Al4V under nano-graphene mixed dielectric: A detailed roughness analysis. *Int. J. Adv. Manuf. Technol.* **2022**, *120*, 7375–7388. [CrossRef]
48. Chandra, K.S.; Sarkar, D. Structural properties of Al_2O_3–MgO–C refractory composites improved with YAG nanoparticle hybridized expandable graphite. *Mater. Sci. Eng. A* **2021**, *803*, 140502. [CrossRef]
49. Gong, S.; Cheng, X.; Li, Y.; Wang, X.; Wang, Y.; Zhong, H. Effect of nano-SiC on thermal properties of expanded graphite/1-octadecanol composite materials for thermal energy storage. *Powder Technol.* **2020**, *367*, 32–39. [CrossRef]
50. Sun, W.; Hu, R.; Zhang, H.; Wang, Y.; Yang, L.; Liu, J.; Zhu, M. A long-life nano-silicon anode for lithium ion batteries: Supporting of graphene nanosheets exfoliated from expanded graphite by plasma-assisted milling. *Electrochim. Acta* **2016**, *187*, 1–10. [CrossRef]
51. Karami, B.; Azimi, N.; Ahmadi, S. Increasing the electrical efficiency and thermal management of a photovoltaic module using expanded graphite (EG)/paraffin-beef tallow-coconut oil composite as phase change material. *Renew. Energy* **2021**, *178*, 25–49. [CrossRef]

52. Sheth, M.; Gajjar, K.; Jain, A.; Shah, V.; Patel, H.; Chaudhari, R.; Vora, J. Multi-objective optimization of inconel 718 using Combined approach of taguchi—Grey relational analysis. In *Advances in Mechanical Engineering: Select Proceedings of the ICAME 2020*; Springer: Singapore, 2021; pp. 229–235.
53. Wankhede, V.; Jagetiya, D.; Joshi, A.; Chaudhari, R. Experimental investigation of FDM process parameters using Taguchi analysis. *Mater. Today Proc.* **2020**, *27*, 2117–2120. [CrossRef]
54. Chaudhari, R.; Patel, H.; Sheth, M.; Prajapati, N.; Fuse, K.; Abhishek, K.; Vora, J. Effect of different tool electrodes (wire) of WEDM process of inconel 718. In *Recent Advances in Mechanical Infrastructure: Proceedings of the ICRAM 2021*; Springer: Singapore, 2022; pp. 317–327.
55. Patel, V.K.; Savsani, V.J. Heat transfer search (HTS): A novel optimization algorithm. *Inf. Sci.* **2015**, *324*, 217–246. [CrossRef]
56. Galati, M.; Antonioni, P.; Calignano, F.; Atzeni, E. Experimental Investigation on the Cutting of Additively Manufactured Ti6Al4V with Wire-EDM and the Analytical Modelling of Cutting Speed and Surface Roughness. *J. Manuf. Mater. Process.* **2023**, *7*, 69. [CrossRef]
57. Vora, J.; Shah, Y.; Khanna, S.; Chaudhari, R. Effect of Near-Dry WEDM Process Variables through Taguchi-based-GRA Approach on Performance Measures of Nitinol. *J. Manuf. Mater. Process.* **2022**, *6*, 131. [CrossRef]
58. Pratiwi, D.K.; Arifin, A.; Mardhi, A. Investigation of Welding Parameters of Dissimilar Weld of SS316 and ASTM A36 Joint Using a Grey-Based Taguchi Optimization Approach. *J. Manuf. Mater. Process.* **2023**, *7*, 39. [CrossRef]
59. Chaudhari, R.; Kevalramani, A.; Vora, J.; Khanna, S.; Patel, V.K.; Pimenov, D.Y.; Giasin, K. Parametric optimization and influence of near-dry WEDM variables on nitinol shape memory alloy. *Micromachines* **2022**, *13*, 1026. [CrossRef]
60. Rashwan, S.S.; Abdelkader, B.; Abdalmonem, A.; Abou-Arab, T.W.; Nemitallah, M.A.; Habib, M.A.; Ibrahim, A.H. Experimental and Statistical ANOVA Analysis on Combustion Stability of $CH_4/O_2/CO_2$ in a Partially Premixed Gas Turbine Combustor. *J. Energy Resour. Technol.* **2022**, *144*, 062301. [CrossRef]
61. Shanmugam, B.K.; Vardhan, H.; Raj, M.G.; Kaza, M.; Sah, R.; Hanumanthappa, H. Regression modeling and residual analysis of screening coal in screening machine. *Int. J. Coal Prep. Util.* **2022**, *42*, 2849–2864. [CrossRef]
62. Tharian, B.; Kumar, M.; Dhanish, P.; Manu, R. Effect of Peak Current on Material Removal Rate During EDM of Ti–6Al–4V Using Cold Treated Brass Electrode. In *Advances in Forming, Machining and Automation: Select Proceedings of the AIMTDR 2021*; Springer: Singapore, 2022; pp. 243–251.
63. Sahoo, R.; Debnath, T.; Patowari, P.K. Machinability characteristics of titanium diamond using EDM and its parametric optimization. *Mater. Manuf. Process.* **2023**, *38*, 78–88. [CrossRef]
64. Chaudhari, R.; Vora, J.J.; Patel, V.; López de Lacalle, L.; Parikh, D. Surface analysis of wire-electrical-discharge-machining-processed shape-memory alloys. *Materials* **2020**, *13*, 530. [CrossRef] [PubMed]
65. Goyal, A.; Pandey, A.; Rahman, H.U. Present and future prospective of shape memory alloys during machining by EDM/wire EDM process: A review. *Sādhanā* **2022**, *47*, 217. [CrossRef]
66. Chaudhari, R.; Sheth, M.; Patel, H.; Fuse, K.; Ayesta, I.; de Lacalle, L.L.; Vora, J. Multi-response optimization of alumina powder-mixed WEDM process using taguchi-TOPSIS approach of nitinol SMA. In *Recent Advances in Mechanical Infrastructure: Proceedings of the ICRAM 2021*; Springer: Singapore, 2022; pp. 359–367.
67. Sahu, D.R.; Mandal, A. Critical analysis of surface integrity parameters and dimensional accuracy in powder-mixed EDM. *Mater. Manuf. Process.* **2020**, *35*, 430–441. [CrossRef]
68. Chaudhari, R.; Ayesta, I.; Doshi, M.; Khanna, S.; Patel, V.K.; Vora, J.; López de Lacalle, L.N. Implementation of Passing Vehicle Search Algorithm for Optimization of WEDM Process of Nickel-Based Superalloy Waspaloy. *Nanomaterials* **2022**, *12*, 4394. [CrossRef]
69. Talla, G.; Gangopadhyay, S.; Biswas, C. Influence of graphite powder mixed EDM on the surface integrity characteristics of Inconel 625. *Part. Sci. Technol.* **2017**, *35*, 219–226. [CrossRef]